Shell structure underlying the evolution of quadrupole collectivity in ^{38}S and ^{40}S probed by transient-field g-factor measurements on fast radioactive beams

A. E. Stuchbery,[1] A. D. Davies,[2,3] P. F. Mantica,[2,4] P. M. Davidson,[1] A. N. Wilson,[1,5] A. Becerril,[2,3] B. A. Brown,[2,3] C. M. Campbell,[2,3] J. M. Cook,[2,3] D. C. Dinca,[2,3] A. Gade,[2] S. N. Liddick,[2,4] T. J. Mertzimekis,[2] W. F. Mueller,[2] J. R. Terry,[2,3] B. E. Tomlin,[2,4] K. Yoneda,[2] and H. Zwahlen[2,3]

[1]*Department of Nuclear Physics, The Australian National University, Canberra, ACT 0200, Australia*
[2]*National Superconducting Cyclotron Laboratory, Michigan State University, East Lansing, Michigan 48824, USA*
[3]*Department of Physics and Astronomy, Michigan State University, East Lansing, Michigan 48824, USA*
[4]*Department of Chemistry, Michigan State University, East Lansing, Michigan 48824, USA*
[5]*Department of Physics, The Australian National University, Canberra, ACT 0200, Australia*

(Received 9 August 2006; published 15 November 2006)

The shell structure underlying shape changes in neutron-rich nuclei between $N = 20$ and $N = 28$ has been investigated by a novel application of the transient field technique to measure the first-excited state g factors in ^{38}S and ^{40}S produced as fast radioactive beams. Details of the new methodology are presented. In both ^{38}S and ^{40}S there is a fine balance between the proton and neutron contributions to the magnetic moments. Shell-model calculations that describe the level schemes and quadrupole properties of these nuclei also give a satisfactory explanation of the g factors. In ^{38}S the g factor is extremely sensitive to the occupation of the neutron $p_{3/2}$ orbit above the $N = 28$ shell gap as occupation of this orbit strongly affects the proton configuration. The g factor of deformed ^{40}S does not resemble that of a conventional collective nucleus because spin contributions are more important than usual.

DOI: 10.1103/PhysRevC.74.054307 PACS number(s): 21.10.Ky, 21.60.Cs, 27.30.+t, 27.40.+z

I. INTRODUCTION

In a recent Letter [1] we presented the first application of a high-velocity transient-field (HVTF) technique [2] to measure the g factors of excited states of neutron-rich nuclei produced as fast radioactive beams. Questions on the nature and origins of deformation between $N = 20$ and $N = 28$ were addressed by measuring the g factors of the 2_1^+ states in $^{38}_{16}S_{22}$ and $^{40}_{16}S_{24}$. Figure 1 shows the relevant part of the nuclear chart and indicates the primary beams used to produce the isotopes of interest. In the present article we give a more comprehensive description of the experiment and discuss the interpretation in greater detail. A more technically oriented discussion of the new technique will be published elsewhere [3].

Figure 2 shows the 2_1^+ excitation energies and the $B(E2; 0_1^+ \rightarrow 2_1^+)$ values for the sulfur isotopes. It is apparent from the reduction in the excitation energies of the 2_1^+ states and the increase in $B(E2)$ values that the neutron-rich isotopes between $N = 20$ and $N = 28$ develop collective features. Furthermore, the $N = 28$ nucleus $^{44}_{16}S_{28}$ does not have the high 2_1^+ energy and small $B(E2)$ like the closed-shell $N = 20$ isotope $^{36}_{16}S_{20}$. The data in Fig. 2 together with additional information on the low-excitation level structures imply that the even sulfur isotopes between $N = 20$ and $N = 28$ undergo a transition from spherical at $^{36}_{16}S_{20}$ to prolate deformed in $^{40}_{16}S_{24}$ and $^{42}_{16}S_{26}$ and that the $N = 28$ nucleus $^{44}_{16}S_{28}$ appears to exhibit collectivity of a vibrational character [5–8]. However, the evolution of collective features in these nuclei has underlying causes that remain unclear. Some have argued that a weakening of the $N = 28$ shell gap is important [8,9], whereas others have opined that the effect of adding *neutrons* to the $f_{7/2}$ orbit is primarily to reduce the *proton* $s_{1/2}$-$d_{3/2}$ gap and that a weakening of the $N = 28$ shell gap is not needed to explain the observed collectivity near ^{44}S [10]. There have been several theoretical studies discussing the erosion of the $N = 28$ shell closure and the onset of deformation (e.g., Refs. [11,12] and references therein). To help resolve questions on the nature and origins of deformation between $N = 20$ and $N = 28$, we have used a novel technique to measure the g factors of the 2_1^+ states in $^{38}_{16}S_{22}$ and $^{40}_{16}S_{24}$.

The remainder of the article is arranged as follows: Sec. II describes the experimental procedures, including radioactive beam production, targets, and apparatus. The experimental results and details of the data analysis are given in Sec. III. Our shell-model calculations are presented and discussed in Sec. IV.

II. EXPERIMENTAL PROCEDURES

A. Overview

The experiments reported here use transient fields to study neutron-rich nuclei produced as radioactive beams by fast fragmentation. In our approach the nuclear states of interest are excited and aligned by intermediate-energy Coulomb excitation [13]. The nucleus is then subjected to the transient field in a higher velocity regime than has been used previously for moment measurements, which causes the nuclear spin to precess. Finally, the nuclear precession angle, to which the g factor is proportional, is observed via the perturbed γ-ray angular correlation measured using a multidetector array. It is important to note that the transient-field technique has sensitivity to the *sign* of the g factor, which in itself can be a distinguishing characteristic of the state under study, because

 ©2006 The American Physical Society

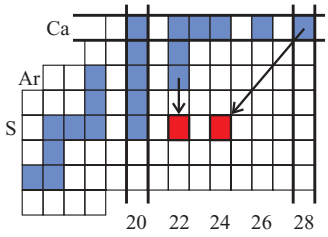

FIG. 1. (Color online) Region of the nuclear chart indicating the primary beam isotopes ^{40}Ar and ^{48}Ca used to produce the ^{38}S and ^{40}S secondary beams (red). The $N = 20, 28$ closed shells are shown outlined in black. Stable isotopes are shaded (blue).

the signs of the spin contributions to the proton and the neutron g factors are opposite.

The transient field (TF) is a velocity-dependent magnetic hyperfine interaction experienced by the nucleus of a swift ion as it traverses a magnetized ferromagnetic material [14,15]. For light ions $Z \lesssim 16$) the maximum TF strength is reached when $v = Zv_0$, i.e., the ion velocity v matches the K-shell electron velocity Zv_0 ($v_0 = c/137$, Bohr velocity). Because the transient field arises from polarized electrons carried by the moving ion its strength falls off as the ion velocity exceeds Zv_0 and the ion becomes fully stripped; a transient-field interaction will not occur for fast radioactive beams with energies near 100 MeV/nucleon until most of that energy is removed. Thus slowing the fast fragment beams to velocities where the transient field can be effective is an essential feature of the measurement.

B. Radioactive beam production and properties

The experiment was conducted at the Coupled Cyclotron Facility of the National Superconducting Cyclotron Laboratory at Michigan State University. Secondary beams of ^{38}S and ^{40}S were produced from 140 MeV/nucleon primary beams

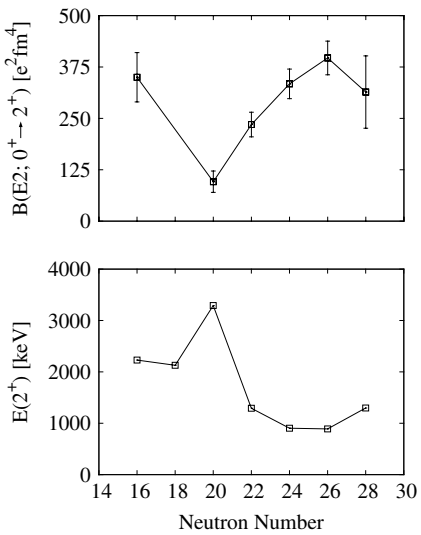

FIG. 2. Previously measured $E(2^+)$ and $B(E2)$ values for the sulfur isotopes [4].

TABLE I. Production and properties of radioactive beams.

Primary beam		Secondary beam			
Ion	Intensity (pnA)	Ion	E (MeV)	Intensity (pps)	Purity (%)
^{40}Ar	25	^{38}S	1547.5	2×10^5	>99
^{48}Ca	15	^{40}S	1582.5	2×10^4	>95

of ^{40}Ar and ^{48}Ca, respectively, directed onto a $\sim$1 g/cm^2 ^{9}Be fragmentation target at the entrance of the A1900 fragment separator [16]. An (971-mg/cm^2) acrylic wedge degrader and a 0.5% momentum slit at the dispersive image of the A1900 were employed. The wedge degrader allowed the production of highly pure beams and also reduced the secondary beam energy to $\sim$40 MeV/nucleon. Further details of the radioactive beams are given in Table I. The ^{38}S (^{40}S) measurement ran for 81 (68) h. The 40 MeV/nucleon beams were made incident on a target consisting of contiguous layers of Au and Fe, 355 mg/cm^2 thick and 110 mg/cm^2 thick, respectively.

C. Target design and test

Prior to the transient-field measurement a test run was performed to ensure that the fast fragment beams at $\sim$40 MeV/nucleon would be slowed to the appropriate velocity regime in the target layers and emerge from the target for downstream detection without severe energy straggling. A 1540-MeV ^{38}S beam was used for this purpose.

Three targets were mounted, in turn, on a rotating target ladder and the energy distribution of the emerging ions was measured with a 980-μm PIN detector placed 41 cm downstream of the target. The targets were (i) the 355 mg/cm^2 Au foil alone, (ii) the Au (355 mg/cm^2) + Fe (100 mg/cm^2) target, and (iii) the Au (355 mg/cm^2) + Fe (110 mg/cm^2) target, which was subsequently chosen for the g-factor measurement. The angle between the target and the beam was varied to effectively increase the target thickness. The transmission of the beam through the target and the energy distribution of the transmitted ions were measured using the PIN detector. These measurements indicated that the Ziegler (1985) stopping powers [17] for sulfur in Au and Fe targets were accurate to about $\pm$5%, although they tend to underestimate the stopping in the Au layer of the target and overestimate the stopping in the Fe layer.

The effect of the energy width of the radioactive beam on the spectrum of the emergent ions is examined in Fig. 3, which compares the particle spectrum measured in the test run for the Au + Fe (100 mg/cm^2) target with Monte Carlo simulations made with the code GKINT_MCDBLS [18]. In the simulations the energy spread of the beam was treated as a Gaussian distribution with its width specified by the full width at half maximum (FWHM). In the case shown in Fig. 3 the sulfur fragments emerged with energies in the range from $\sim$80 to $\sim$200 MeV. A similar post-target energy distribution was observed in the g-factor measurements where both the

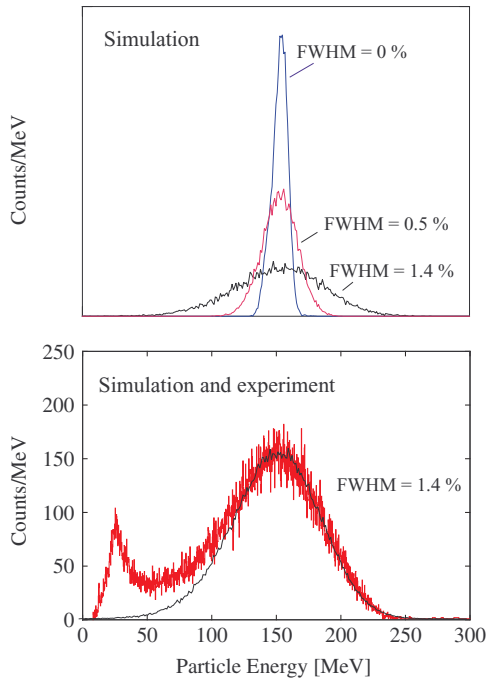

FIG. 3. (Color online) Spectrum of 1540 MeV ^{38}S beam particles after passing through 355 mg/cm^2 of Au followed by 100 mg/cm^2 of Fe. The upper panel shows simulations that examine the effect of the energy width of the ^{38}S beam, which is assumed to have a Gaussian distribution about 1540 MeV with a specified full width at half maximum (FWHM). These simulated spectra all have the same number of events. The experimental spectrum in the lower panel agrees with the simulations that assume the beam energy has a Gaussian distribution with a FWHM of 1.4% (i.e., a standard deviation of 0.5%). The equivalent momentum width is $\Delta p/p = 0.7\%$.

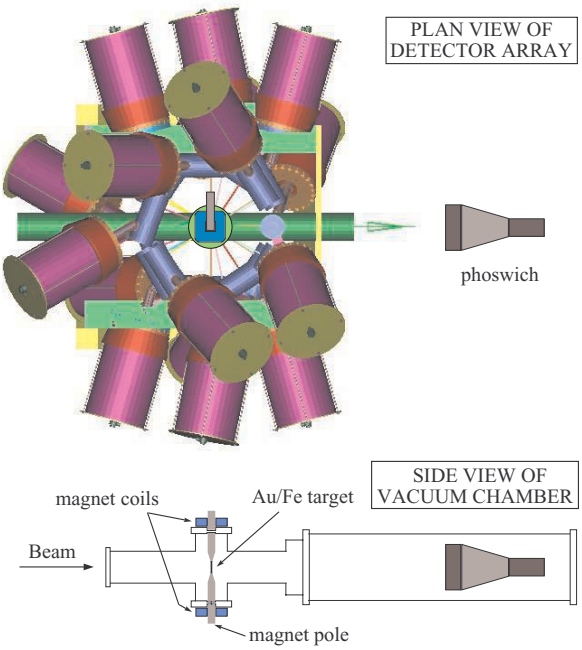

FIG. 4. (Color online) Overhead view of the SeGA detectors and side view of the target chamber showing the magnet, target, and phoswich detector. Projectiles were detected in the downstream phoswich detector.

beam energy and the thickness of the Fe layer were increased slightly. It is evident from Fig. 3 that most of this energy spread stems from the energy width of the radioactive beam, which is determined largely by the momentum acceptance, $\Delta p/p = 0.5\%$ (FWHM), set at the dispersive image slits of the A1900 spectrometer.

D. Apparatus

Figure 4 shows the experimental arrangement. The radioactive beams were delivered onto the Au + Fe target, which had dimensions 30 × 30 mm^2. The target was held between the pole tips of a compact electromagnet that provided a magnetic field of 0.11 T, sufficient to fully magnetize the Fe layer. As the iron layer of the target is much thicker than those typically used in transient-field g-factor measurements, the magnetization of a piece was measured using the Rutgers magnetometer [19]. Fields of 0.062 T were sufficient to ensure saturation. To minimize possible systematic errors, the external magnetic field was automatically reversed every 600 s.

Table II summarizes the properties of the 2_1^+ states and the key aspects of the energy loss of the sulfur beams in the target, applicable for the g-factor measurements. The high-Z Au target layer serves to enhance the Coulomb excitation yield and slow the projectiles to under 800 MeV; the thick iron layer results in a long interaction time with the transient field, maximizing the spin precession. The energies $\langle E_i \rangle$, with which the sulfur ions enter the iron layer, were calculated taking into account the energy loss measurements for the Au layer alone, whereas the energies $\langle E_e \rangle$, with which the ions emerge from the iron layer into vacuum, were determined from the Doppler shifts observed in the g-factor measurements.

TABLE II. Nuclear parameters and reaction kinematics. $B(E2)\uparrow = B(E2; 0^+_{gs} \rightarrow 2^+_1)$. $\langle E_{i,e} \rangle$ and $\langle v_{i,e} \rangle$ are the ion kinetic energies and velocities at the entrance and exit of the iron layer. The effective transient-field interaction time $t_{\rm eff}$ is evaluated for ions that decay after leaving the target.

Isotope	E(2_1^+) (keV)	$B(E2)\uparrow$ (e^2fm^4)	$\tau(2_1^+)$ (ps)	$\langle E_i \rangle$ (MeV)	$\langle E_e \rangle$ (MeV)	$\langle v_i/Zv_0 \rangle$	$\langle v_e/Zv_0 \rangle$	$t_{\rm eff}$ (ps)
^{38}S	1292	235(30)	4.9	762	123	1.75	0.71	2.98
^{40}S	904	334(36)	21	782	145	1.73	0.75	2.99

Projectiles scattered forward out of the target were detected with a 15.24-cm-diameter plastic scintillator phoswich detector placed 79.2 cm downstream of the target position. The phoswich detector consisted of a 750-μm layer of fast BC-400 scintillator and a 5.08-cm layer of slow BC-444 scintillator. The maximum scattering angle, 5.5°, limits the distance of closest approach to near the nuclear interaction radius in both the Au and Fe target layers. Positioning the particle detector downstream also lowers the exposure of the γ-ray detectors to the radioactive decay of the projectiles.

Although the sulfur fragments do not penetrate beyond the fast scintillator, the slow scintillator helps discriminate against more penetrating radiation such as light ions produced in the secondary target, or accompanying the beam, and β decays in the phoswich from the decay of the implanted radioactive beam. Along with the fast-slow particle identification information from the phoswich, the particle time-of-flight was also recorded with respect to the cyclotron RF. Triggers from the radioactive decay of the beam particles, which are much lower in energy than the beam particles, were minimized by raising the threshold of the phoswich discriminator.

For the ^{38}S run, a circular Pb mask was placed on the phoswich detector to block particles in the range $0° \leqslant \theta \leqslant 2.5°$ and hence lower the count rate by excluding those scattering angles where the Rutherford cross section is large but the Coulomb excitation cross section is small. The mask helped reduce random particle-γ coincidences and pileup events in the phoswich detector. No mask was used for the ^{40}S run because the particle rate was low enough for pileup to be negligible.

To detect de-excitation γ rays, the target chamber was surrounded by 14 HPGe detectors of the segmented germanium array (SeGA) [20]. The SeGA detectors were positioned with the crystal centers 24.5 cm from the target position. Six pairs of detectors were fixed at symmetric angles $(\pm\theta, \phi) = (29°, 90°)$, $(40°, 131°)$, $(60°, 61°)$, $(139°, 46°)$, $(147°, 143°)$, and $(151°, 90°)$, where θ is the polar angle with respect to the beam axis and ϕ is the azimuthal angle measured from the vertical direction, which coincides with the magnetic field axis. Figure 5 indicates the coordinate frame and definitions of the angles. To make a connection with the notation used for conventional transient-field measurements [14,15], the locations of the pair of detectors at the spherical polar angles (θ, ϕ) and $(\theta, \phi + 180°)$ are written as $(\pm\theta, \phi)$; thus if $(+\theta, \phi) = (|\theta|, \phi)$, then $(-\theta, \phi) = (|\theta|, \phi + 180°)$. Each $\pm\theta$ pair is in a plane that passes through the center of the target.

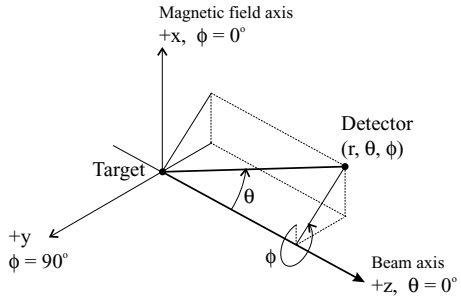

FIG. 5. Coordinate systems used in the present experiment and its analysis.

Two additional detectors were placed at $(\theta, \phi) = (90°, 112°)$ and $(24°, 0°)$ to assist the measurement of the angular correlation. All 14 detectors were used to measure the γ-ray angular correlations concurrently with the precessions. Because the precession angles are small, the unperturbed angular correlation can be reconstructed by adding the data for the two directions of the applied magnetic field.

The positions of the SeGA detectors with respect to the target position were measured to an accuracy of 2 mm using a theodolite system. This information was used to find the actual crystal locations in conjunction with the SeGA crystal segment positions measured by Miller *et al.* [21]. The 32-fold segmentation of the detectors improves the position determination of the γ ray from the entire crystal length (8 cm) to near the segment length (1 cm), which is needed for Doppler corrections due to the high velocity of the emitting nuclei. The angle of γ-ray emission was deduced from the position of the detector segment that registered the highest energy deposition. With this algorithm the position resolution is near (but does not reach) the segment length.

The master trigger for the data acquisition was set to record particle-γ coincidences as well as down-scaled particle singles. Thirty-three energy signals were recorded for each γ-ray detector, corresponding to the 32 segments and the central contact. To differentiate between the signals from the fast and slow scintillator, the pulse from the phoswich detector was charge integrated over the whole signal and over the tail (slow) part of the signal in separate QDC channels. Time differences were recorded between the phoswich detector and the γ-ray detectors. To assist with particle identification, the time-of-flight spectrum was also recorded for particles striking the phoswich detector. Finally, each event included a tag that identified the direction of the external magnetic field.

III. EXPERIMENTAL RESULTS AND ANALYSIS

A. Particle and γ-ray spectra

A particle identification plot obtained with the phoswich detector during the ^{38}S measurement is shown in Fig. 6. This spectrum was obtained by plotting the integrated charge for the slow (or tail) part of the phoswich signal versus the integrated charge for the whole signal. Most of the intensity corresponds

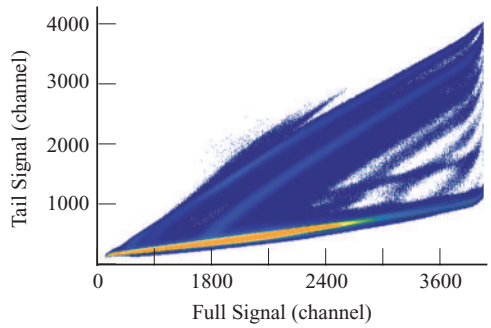

FIG. 6. (Color online) Phoswich particle identification plot recorded during the ^{38}S run. Pulse-shape discrimination was obtained by plotting the integrated charge for the slow (tail) signal versus the full charge-integrated signal.

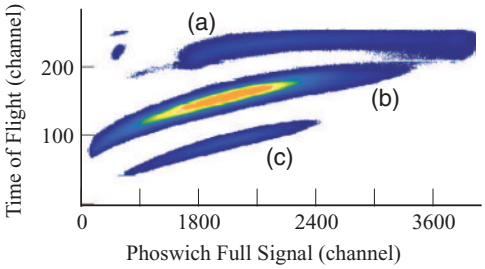

FIG. 7. (Color online) Time-of-flight (between the cyclotron RF and the phoswich detector) versus the phoswich energy recorded during the ^{38}S run. The labeled features are (a) light particles registered in the slow scintillator, (b) ^{38}S ions in coincidence with γ rays, and (c) downscaled events. See text for further details.

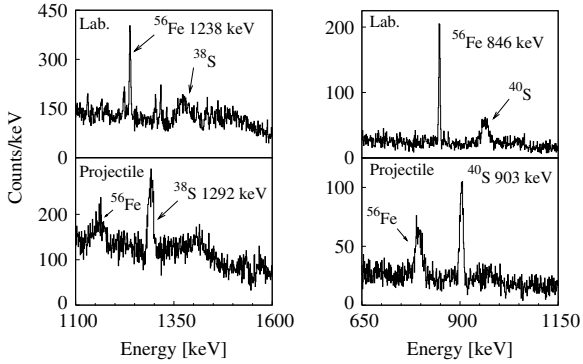

FIG. 8. Random-subtracted lab frame (top) and Doppler-corrected (bottom) γ-ray spectra at $\theta = 40^\circ$ for ^{38}S (left) and ^{40}S (right). The sulfur and iron peaks are labeled. The broad feature to the right of the 1292-keV line is mainly its Doppler tail, due to decays within the target, although there is a contribution from a contaminant line as well. The line at 1238 keV is the $4 \rightarrow 2$ transition emitted by ^{56}Fe nuclei at rest.

to the sulfur projectiles. It has a small tail component and therefore occurs in a band located along the full signal axis. The upsloping lines of intensity that deviate from this heavy-ion band are due to low-Z particles that punch through into the slow scintillator. Such ions accompany the beam, probably originating at the acrylic Image-2 wedge in the A1900 spectrometer; they are not predominantly produced in the secondary target.

The spectrum in Fig. 7 shows the time-of-flight between the cyclotron radio frequency (RF) and the phoswich trigger pulse versus the phoswich energy signal (integration of the full pulse shape). Three distinct features are evident in this spectrum. The upper feature, labeled (a), corresponds to events that cause a large amount of slow scintillation in the phoswich; they are the light particles discussed already. The middle region, labeled (b), corresponds to phoswich events triggered by sulfur projectiles that are in coincidence with γ rays, and the lower region, labeled (c), is made up of downscaled phoswich events. (The downscaler module introduces an additional delay that shifts this group of events away from the phoswich-γ coincidences.)

Gamma-ray spectra gated on sulfur recoils were produced and corrected for random coincidences by subtracting spectra gated on the appropriate regions of the particle-γ time spectra. Both the particle identification and time-of-flight information from the phoswich were used to select the events of interest. Spectra were also created for each γ-ray detector and for each direction of the magnetic field (up/down). Examples of the random-subtracted spectra for the lab frame are given in the upper panels of Fig. 8. From the measured Doppler shift of the deexcitation γ rays in the laboratory frame, the average after-target ion velocities were determined to be 0.083 c for ^{38}S and 0.088 c for ^{40}S (i.e., $v/Zv_0 = 0.71$ and 0.75, respectively). The velocity distribution of the exiting ^{40}S ions was also measured by shifting the phoswich detector by ± 15 cm from its normal position and observing the change in the flight times of the projectiles. These procedures firmly establish that the sulfur ions were slowed through the peak of the TF strength at Zv_0 into the region where it has been well characterized [2,15].

Doppler-corrected spectra were also produced using the angular information from the SeGA detector segments and the particle energy information from the phoswich detector on an event-by-event basis, which is essential because of the spread in particle velocities. The lower panels of Fig. 8 show examples of the Doppler-corrected γ-ray spectra. The peak to background ratio seems to be better for the ^{40}S measurement because (i) there are more counts in the ^{38}S measurement, which gives an overall higher count baseline, and (ii) the combination of the higher γ-ray energy and shorter level lifetime in ^{38}S results in a broader Doppler-corrected peak.

Most of the excited nuclei decay in vacuum after leaving the target material; however, for ^{38}S a significant number also decay at higher velocities, extending up to the secondary beam velocity, while still within the target. The long Doppler tail becomes almost indistinguishable from background at extreme forward and backward angles but is clear at $\theta = 40^\circ$, 60°, and 90°. It was established through Doppler broadened line shape (DBLS) calculations based on a Monte Carlo approach that the angular correlations and nuclear precessions can be determined accurately by an analysis of the vacuum-flight peak alone, without the need to include the Doppler tail. Examples of the DBLS calculations and comparisons with the experimental spectra are shown in Fig. 9. From these spectra it can be seen that the proportion of the γ-ray peak that corresponds to decays within the target is very small and only weakly dependent on the detection angle. Note that the present calculations of the line shapes do not account for the possibility that a γ-ray event may be assigned to the wrong segment of the detector. Having established that the correct angular correlation and g-factor results are obtained by analyzing only the γ-ray peak, and excluding the tail, no attempt was made to obtain a quantitative fit to the observed γ-ray line shapes. Further details of these calculations are given below and elsewhere [18].

The 2^+ peak areas averaged 925 counts/detector per field direction for ^{38}S and 400 counts/detector per field direction for ^{40}S, in each of the six angle pairs of SeGA detectors used for extracting the precessions.

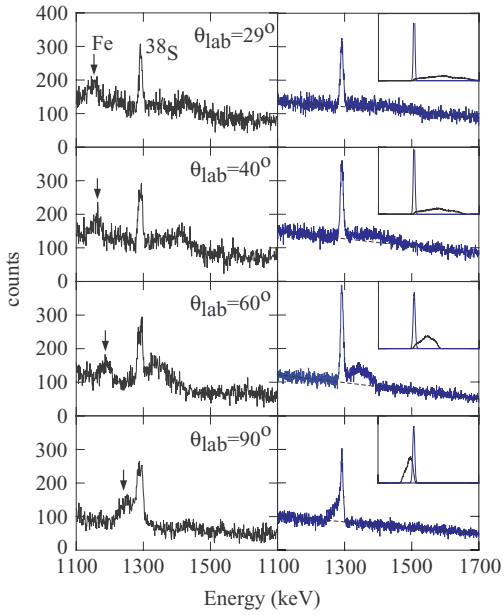

FIG. 9. (Color online) Random-subtracted Doppler-corrected γ-ray spectra from the ^{38}S measurement are shown on the left. The 1238-keV line emitted by ^{56}Fe nuclei at rest in the lab frame is shifted towards the ^{38}S peak by the Doppler correction as the detection angle approaches 90°. The right panels show simulated spectra used to evaluate the impact of the Doppler broadened line shape on the angular correlation and precession measurements. The insets show the energy range from 1150 to 1550 keV. These simulations, which do not include background, indicate the relative contributions of decays in the target (broad peak) and decays in vacuum (sharp peak), which overlap. The experimental peak is broader than that in the simulations because a simplified model is used for the γ-ray detectors.

B. Angular correlations and precessions

In the rest frame of the nucleus, the perturbed angular correlation is given by

$$W(\theta,\phi,\pm\Delta\Theta) = 4\pi \sum_{k,q} \frac{a_k Q_k G_k}{(2k+1)}(-1)^q \times Y^k_q(|\Delta\Theta|,\pm\pi/2) Y^k_{-q}(\theta,\phi), \quad (1)$$

where (θ,ϕ) are the spherical polar angles at which the γ ray is detected and $\pm\Delta\Theta$ is the transient-field precession angle for the two directions of the magnetic field; $k = 0, 2, 4$, and q takes integer values such that $-k \leqslant q \leqslant k$. As shown in Fig. 5, the beam direction defines $\theta = 0$ and the magnetic-field direction defines $\phi = 0$. The unperturbed angular correlation has symmetry about the beam axis and reduces to the ϕ-independent form:

$$W(\theta) = 1 + \sum_{k=2,4} a_k Q_k G_k P_k(\cos\theta). \quad (2)$$

The a_k coefficients, which depend on the particle detector geometry, the spins of the initial and final nuclear states and the multipolarity of the γ-ray transition, can be evaluated from the theory of Coulomb excitation [22]. The correction factors for the finite solid angles of the γ-ray detectors, Q_k, are near unity in the present work. The deorientation coefficients, G_k, account for the effect of hyperfine fields experienced by ions that recoil into vacuum carrying atomic electrons.

These recoil in vacuum effects were evaluated based on measured charge-state fractions for sulfur ions emerging from iron foils with energies between 92 and 236 MeV [23]. The large free-ion hyperfine interactions of hydrogen- and lithium-like ions [24], which quickly reach hard-core values for nuclear lifetimes of a picosecond or more, are dominant. To a good approximation, the deorientation coefficients can be expressed as $G_k = 1 - (Q_H + Q_{\rm Li})b_k$, where the fraction of ions with one and three electrons is $Q_H + Q_{\rm Li}$ and $b_k = k(k+1)/(2I+1)^2$ for nuclear spin I and $k = 2, 4$. Using the measured charge-state fractions gives $G_2 = 0.90$ and $G_4 = 0.65$.

The angular correlations were calculated with the program GKINT [25]. For each layer of the target, the code GKINT performs integrals over the solid angle of the particle detector and over the energy loss of the beam in the target. The average a_k coefficients, for example, are evaluated as

$$\langle a_k \rangle = \frac{2\pi}{\langle \sigma \cdot t_{\rm tgt} \rangle} \int_0^{t_{\rm tgt}} \int_{\theta_p^{\rm min}}^{\theta_p^{\rm max}} a_k(\theta_p, E[z]) \times \frac{d\sigma}{d\Omega}(\theta_p, E[z]) \sin\theta_p d\theta_p dz, \quad (3)$$

where

$$\langle \sigma \cdot t_{\rm tgt} \rangle = 2\pi \int_0^{t_{\rm tgt}} \int_{\theta_p^{\rm min}}^{\theta_p^{\rm max}} \frac{d\sigma}{d\Omega}(\theta_p, E[z]) \sin\theta_p d\theta_p dz, \quad (4)$$

where $d\sigma(\theta_p, E[z])/d\Omega$ denotes the Coulomb excitation cross section as a function of the scattering angle θ_p and the projectile energy $E[z]$, which varies with the depth z through the target layer. The integrals are evaluated numerically using Simpson's rule. To evaluate other average quantities of interest such as the average energy of excitation, or the average transient-field precession, the quantity to be averaged replaces a_k in an expression of the same form as Eq. (3).

Comparisons between the experimental and theoretical angular correlations are made in Fig 10. To indicate the effect of the Lorentz transformation (see, e.g., Refs. [26,27]) the angular correlations are shown in both the laboratory frame and the projectile frame. Good agreement was found between the calculated γ-ray angular correlations and the data.

To describe the procedure for the extraction of the nuclear precession angle $\Delta\Theta$ it is helpful to begin with the four detectors in the plane through the target that is perpendicular to the magnetic field direction, as illustrated in Fig. 11. For these detectors $\Delta\Theta = \Delta\theta$ and the data analysis is identical to that in a conventional transient-field g-factor measurement [14,15,28,29]. The magnetic field causes a rotation of the angular correlation pattern around the x axis, with positive precession angles for a right-handed coordinate frame in the direction indicated. Thus to first order in $\Delta\Theta$ we have

$$W\uparrow\downarrow = W(\theta \mp \Delta\Theta) \simeq W(\theta) \mp \Delta\Theta \frac{dW}{d\theta}, \quad (5)$$

where the arrows indicate the direction of the external magnetic field. The precession angle is then determined from the double ratio of counts in a pair of detectors for each field direction. Considering, for example, the pair of detectors labeled 1 and

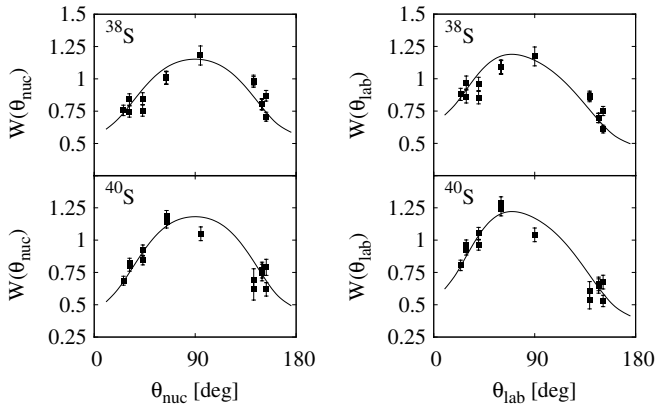

FIG. 10. Angular correlations for ^{38}S and ^{40}S. The left panels show the angular correlation in the frame of the projectile nucleus, whereas the right panels show the same angular correlations in the lab frame. The Lorentz boost causes a shift in the effective detection angle and an angle-dependent change in the solid angle. Data are normalized to the calculated angular correlation. The difference in anisotropy stems from the alignment produced by Coulomb excitation, which depends on the ratio of $E(2^+)$ to the beam velocity (i.e., the adiabacity parameter, ξ, see Ref. [22] and references therein.)

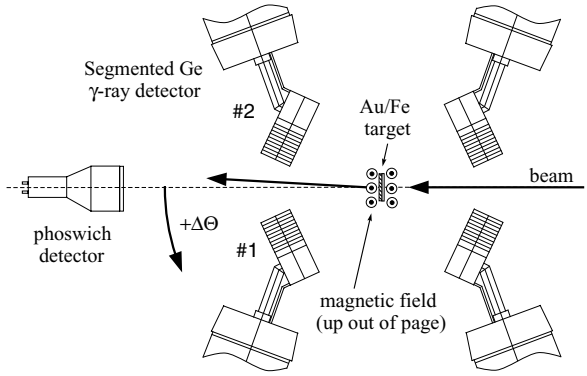

FIG. 11. Schematic view of the experimental arrangement from above showing only the four SeGA detectors perpendicular to the magnetic field axis. The direction of positive precession angles, $\Delta\Theta$, is indicated.

2 in Fig. 11, the relevant experimental double ratio ρ is

$$\rho = \sqrt{\frac{N_1 \uparrow}{N_1 \downarrow} \cdot \frac{N_2 \downarrow}{N_2 \uparrow}}. \tag{6}$$

Because the detector efficiencies and running times cancel out, ρ and $\Delta\Theta$ are related by

$$\rho = \frac{1 - S(\theta)\Delta\Theta}{1 + S(\theta)\Delta\Theta}, \tag{7}$$

where

$$S(\theta) = \frac{1}{W}\frac{dW}{d\theta}\bigg|_{\theta}. \tag{8}$$

It is conventional to define the "effect,"

$$\epsilon = (1 - \rho)/(1 + \rho), \tag{9}$$

so that

$$\Delta\Theta = \epsilon/S. \tag{10}$$

These expressions apply only for the four detectors in the $\phi = 90^\circ$ (horizontal) plane. We now generalize to include the detector pairs that are not in this plane. By expanding Eq. (1) to first order in $\Delta\Theta$ it can be shown that

$$W \uparrow\downarrow = W(\theta, \phi, \mp\Delta\Theta) \simeq W(\theta) \mp \Delta\Theta \sin\phi \frac{dW}{d\theta}. \tag{11}$$

It follows that data analysis for a pair of detectors placed at the spherical polar angles (θ, ϕ) and $(\theta, \phi + 180^\circ)$ can proceed exactly as in the familiar case, but with the definition

$$S(\theta, \phi) = S(\theta) \sin\phi. \tag{12}$$

Finally, it remains to note that the effect of the Lorentz transformation must be taken into account by evaluating S at the appropriate angle in the rest frame of the nucleus that corresponds to the laboratory detection angle [25].

The precession results are summarized in Table III. The two pairs of detectors at $\theta = 29^\circ$ and 151°, which were located in the horizontal plane perpendicular to the external magnetic field direction, near the angle of maximum slope of the γ-ray angular correlation, are most sensitive to the nuclear precession.

To cover the uncertainties in the recoil in vacuum corrections and the possibility that some nuclear interference might affect the Coulomb excitation process for the (small) fraction of collisions that approach the nuclear interaction radius, an uncertainty of $\pm 10\%$ has been assigned to the S values.

TABLE III. Precession results.

Detectors				^{38}S			^{40}S		
Pair	θ°	ϕ_1°	ϕ_2°	ϵ ($\times 10^3$)	S	$\Delta\Theta$ (mrad)	ϵ ($\times 10^3$)	S	$\Delta\Theta$ (mrad)
1	29	270	90	−50(20)	+0.79(8)	−64(27)	−17(35)	+0.86(9)	−20(41)
2	151	270	90	+26(23)	−0.80(8)	−33(29)	−4(35)	−0.88(9)	+5(40)
3	139	226	46	−10(23)	−0.54(5)	+19(43)	+7(28)	−0.58(6)	−12(48)
4	147	323	143	−7(27)	−0.48(5)	+15(57)	−24(31)	−0.52(5)	+46(60)
5	40	311	131	−41(19)	+0.50(5)	−83(39)	+26(32)	+0.53(5)	+49(60)
6	60	241	61	−18(15)	+0.26(3)	−69(58)	+1(28)	+0.27(3)	+4(103)
Average						−43(15)			+5(21)

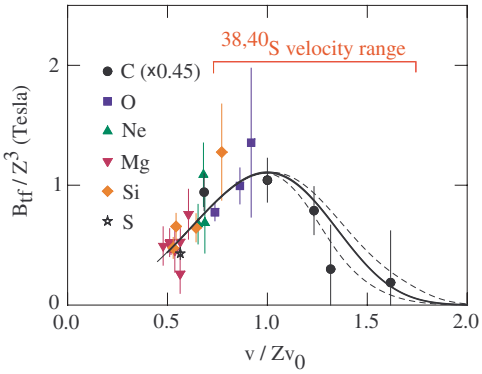

FIG. 12. (Color online) Transient field parametrization (solid line) for high-velocity light ions from Ref. [2]. Data points are measured transient-field strengths reported in the literature. See Refs. [2,15,30] for further details and references.

C. Transient-field calibration and *g* factor results

An evaluation of

$$\Delta\Theta/g = (-\mu_N/\hbar)\int B_{\rm tf}dt \qquad (13)$$

is required to extract the experimental g factors. For light ions ($Z \leqslant 16$) traversing iron and gadolinium hosts at high velocity, the dependence of the TF strength on the ion velocity, v, and atomic number, Z, can be parametrized [2,30] as

$$B_{\rm tf}(v, Z) = AZ^P(v/Zv_0)^2\, e^{-\frac{1}{2}(v/Zv_0)^4}, \qquad (14)$$

where $v_0 = c/137$ is the Bohr velocity. This is a model-based parametrization that takes account of the known physics of the transient field (see Refs. [2,15,30] and references therein). A fit to data for iron hosts yielded $A = 1.82(5)$ T with $P = 3$ [2]. The experimental data and the adopted parametrization are shown in Fig. 12. The velocity range sampled in the present experiments is also indicated. Although the data are sparse in the high-velocity region, there can be no dispute about the general trend and that the maximum TF strength is reached when the ion velocity matches the K-shell electron velocity, $v = Zv_0$. Also shown in Fig. 12 are two alternative parametrizations of the field strength in the region $v > Zv_0$ chosen to give an indication of the uncertainty in the transient-field calibration. Compared with the adopted parametrization, these extrapolations give values of $\Delta\Theta/g$ that differ by $\sim \pm 12\%$.

Calculations of $\Delta\Theta/g$ were performed using the code GKINT to take into account the incoming and exiting ion velocities, the energy- and angle-dependent Coulomb excitation cross sections in both target layers, the excited-state lifetimes, and the parametrization of the TF strength in Eq. (14). The results and the g factors extracted are given in Table IV.

The g factor results are not very sensitive to the somewhat uncertain behavior of the transient field at the highest velocities because (i) the ions spend least time interacting with the TF at high velocity and (ii) the TF strength near $2Zv_0$ is very small. Furthermore, the positive g factor in ^{38}S and the essentially null effect for ^{40}S are both firm observations, independent of the transient-field strength. The g factor of ^{38}S is almost 3 standard deviations from zero.

TABLE IV. Experimental results. The spin precession per unit g factor, $(\Delta\Theta/g)_{\rm calc}$, is evaluated for ions that decay after leaving the target. The experimental g factor is given by $g = \Delta\Theta_{\rm exp}/(\Delta\Theta/g)_{\rm calc}$.

Isotope	$(\Delta\Theta/g)_{\rm calc}$ (mrad)	$\Delta\Theta_{\rm exp}$ (mrad)	g
^{38}S	−330(41)	−43(15)	+0.13(5)
^{40}S	−339(42)	+5(21)	−0.01(6)

The experimental uncertainties assigned to the g factors are dominated by the statistical errors in the γ-ray count ratios, with small contributions from the angular correlation (10%) and transient-field calibration (12%) added in quadrature.

D. Monte Carlo simulations

In the analysis of the data presented above an analytical formalism has been used to evaluate the average angular correlation coefficients, the transient-field precession per unit g factor, and other quantities of interest.

To obtain a more detailed insight into the experiment and data analysis procedures it is helpful to use a Monte Carlo approach to model the experiment. The code GKINT_MCDBLS was written to generate event data for particle-γ coincidences that can be sorted and correlated with calculated quantities such as the transient-field precession. The effect of the energy spread on the incident beam on the particle spectrum beyond the target was discussed above, and examples of the calculated Doppler broadened γ-ray line shapes were presented in Fig. 9. Here we examine the behavior of the precession angle and the angular correlation coefficients a_2 and a_4 as a function of the detected γ-ray energy.

Aside from the statistical uncertainties, which can be minimized by increasing the number of events in the simulation, the Monte Carlo approach allows for a rigorous treatment of the decay-in-flight and vacuum deorientation effects. It also properly includes the contribution to the γ-ray peak that is analyzed to extract the g factor, stemming from excitation in the Au and Fe layers of the target, and that cannot be separated experimentally.

Figure 13 shows how the angular correlation coefficients, a_2 and a_4, and the transient-field precession, $\Delta\Theta/g$, vary as a function of the γ-ray line shape in the laboratory frame. A detector at 29° in the laboratory frame was chosen for this comparison. The bump in the line shape near 1540 keV (lower panel) is due to the change in stopping powers as the ^{38}S ions pass into the Fe layer. As can be seen in the middle panel, there is no transient-field precession in the highest part of the Doppler tail (above the bump). This part of the line shape corresponds to ^{38}S ions that are excited and then decay in the Au layer of the target, before reaching the iron layer. As the sulfur ions slow and decay within the iron layer the transient-field precession $\Delta\Theta/g$ increases, reaching its maximum values for those ions that do not decay until they leave the iron layer and emerge into vacuum. The upper part of Fig. 13 shows the variation of both a_k and a_kG_k, where G_k is the vacuum deorientation coefficient. Clearly, the vacuum

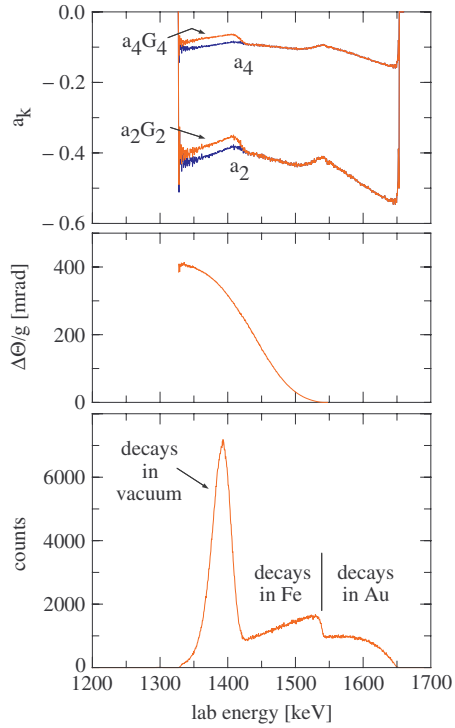

FIG. 13. (Color online) Monte Carlo simulations (10^6 events). (Lower panel) Doppler broadened γ-ray line shape at 29° in the laboratory frame. An equivalent spectrum in the projectile frame is shown in the uppermost panel of Fig. 9. Much of the energy width in the laboratory frame stems from the spread in the projectile velocity, which must be Doppler-corrected event by event using the energy from the phoswich detector (Sec. III A). (Middle panel) The transient-field precession per unit g factor as a function of the emitted γ-ray energy. (Upper panel) Angular correlation coefficients as a function of the emitted γ-ray energy. The effect of vacuum deorientation is indicated by the (red) line labeled a_kG_k.

deorientation effect applies only to those ions that decay in vacuum and hence has an effect only in the peak part of the line shape. Aside from the vacuum deorientation effect, the variation in the magnitude of the a_k coefficients as a function of the Doppler shift has its origin in the alignment produced by intermediate energy Coulomb excitation [22,25]. There is a pronounced dependence on the beam energy, such that the alignment is reduced for those projectiles that are excited after losing energy within the target.

At present the variation of the γ-ray intensity across the acceptance of the detector is not included, and the response of the segmented Ge detector is treated approximately. For example, it is assumed that the hit is always assigned to the correct segment. These approximations are not significant in the present context.

Because the ^{38}S nuclei can be excited in either the Au or Fe layers of the target, and many of them decay before they leave the target and emerge into vacuum, the analytic (GKINT) calculations of a_2G_2, a_4G_4, and $\Delta\Theta/g$ for the vacuum flight peak required some simplifying approximations (mainly to estimate the relative contributions of excitation in the two target layers). The Monte Carlo (GKINT_MCDBLS) calculations, however, enable a simple and rigorous evaluation of these quantities of interest. The disadvantage is that the Monte Carlo calculation is very time consuming. It was found that the difference between the two approaches was small in our case. As well as providing a deeper insight into the experiment, the Monte Carlo calculations therefore support our use of the approximate analytic calculations, which introduce negligible error compared with the statistical uncertainties in the experiment.

IV. SHELL MODEL AND DISCUSSION

A. Shell-model calculations

Shell-model calculations were performed for $^{36}_{16}S_{20}$, $^{38}_{16}S_{22}$, and $^{40}_{16}S_{24}$, and their isotones $^{38}_{18}Ar_{20}$, $^{40}_{18}Ar_{22}$, and $^{42}_{18}Ar_{24}$, using the code OXBASH [31] and the *sd-pf* model space where (for $N \geqslant 20$) valence protons are restricted to the *sd* shell and valence neutrons are restricted to the *pf* shell. The Hamiltonian was that developed in Ref. [32] for neutron-rich nuclei around $N = 28$, i.e., the SDPF-NR interaction [33]. These calculations reproduce the energies of the low-excitation states to within 200 keV. With standard effective charges of $e_p \sim 1.5$ and $e_n \sim 0.5$ they also reproduce the measured $B(E2)$ values. The relevant results for the 2^+_1 states are summarized in Table V, where they are labeled SDPF. For the purposes of the following discussion, the $B(E2)$ and $Q(2^+)$ values are also presented in terms of the equivalent deformation parameter β. These electric quadrupole properties have been calculated and discussed by Retamosa *et al.* [34]. Although the shell-model Hamiltonian has been improved since their work, the theoretical $B(E2)$ and deformation values agree closely with the values in Table V, and their discussion remains relevant.

The g factors of the 2^+_1 states were evaluated using the bare nucleon g factors. The calculated g factors are compared with experimental results in Fig. 14 and Table VI, which also shows the orbital and spin contributions to the g factor originating from both protons and neutrons. As discussed below, the overall level of agreement between theory and experiment is satisfactory given the extreme sensitivity to configuration mixing and the near cancellation of proton and neutron contributions in the $N = 22, 24$ isotones.

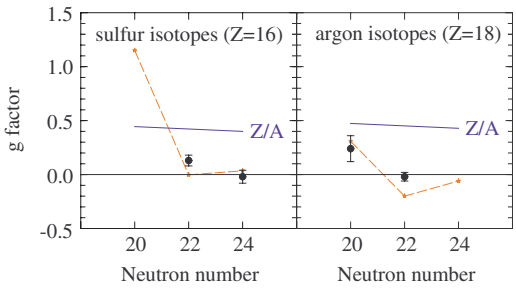

FIG. 14. (Color online) Theoretical g factors compared with experiment. The dashed line shows the present shell-model calculations. The previous results for ^{38}Ar and ^{40}Ar are from Refs. [35] and [36], respectively.

TABLE V. Theoretical and experimental excitation energies, quadrupole moments, and $B(E2)$ values. Experimental data are from Ref. [4].

Nuclide	Model	$E^{th}_{2^+}$ (MeV)	$E^{exp}_{2^+}$ (MeV)	$Q(2^+_1)$ (e fm^2)	$B(E2)\uparrow^{th}$ (e^2 fm^4)	$B(E2)\uparrow^{exp}$ (e^2 fm^4)	β^{th}_Q	$\lvert\beta^{th}_{E2}\rvert$	$\lvert\beta^{exp}_{E2}\rvert$
^{36}S	SDPF	3.426	3.291	−11.6	141	104(28)	+0.21	0.20	0.17(2)
^{38}S	SDPF	1.531	1.292	−9.7	268	235(30)	+0.17	0.26	0.25(2)
	SDF	1.286		+7.5	158		−0.13	0.20	
^{40}S	SDPF	0.980	0.904	−19.3	473	334(36)	+0.33	0.34	0.28(2)
	SDF	1.052		−9.8	328		+0.17	0.28	
^{38}Ar	SDPF	2.018	2.167	+4.3	178	130(10)	−0.07	0.19	0.16(1)
^{40}Ar	SDPF	1.371	1.461	+8.5	263	330(40)	−0.13	0.22	0.25(2)
	SDF	0.966		+12.8	228		−0.20	0.21	
^{42}Ar	SDPF	1.243	1.208	+5.2	360	430(10)	−0.08	0.25	0.28(3)
	SDF	0.918		+13.5	317		−0.20	0.24	

The main partitions of the 2^+_1-state wave functions in ^{38}S and ^{40}S are indicated in Table VII. Table VIII shows the decomposition of the $g(2^+)$ values into the contributions from each combination of single-particle orbitals for ^{38,40}S and ^{38,40}Ar. The off-diagonal contributions from spin-orbit partner orbits can play an important role. In ^{38}S and ^{40}S they tend to quench the (diagonal) moment of the dominant configuration.

Many authors have argued on experimental and theoretical grounds that ^{40}S ($N = 24$) is deformed, some linking it to a weakening of the $N = 28$ shell gap (see Refs. [5–8,11,12, 34] and references therein). To explore the role of excitations across the $N = 28$ shell gap, a further set of calculations was performed in which the neutrons were confined to the $f_{7/2}$ orbit. The results of these calculations, labeled SDF, are given in Tables V and VI.

B. Discussion of results

In the $N = 20$ isotones, ^{36}S and ^{38}Ar, the 2^+_1 state is a pure proton excitation for our model space. In ^{36}S the first-excited state at 3.29 MeV is dominated (87%) by the proton $(s_{1/2}d_{3/2})_{2^+}$ configuration for which $g = +1.459$. The 2^+_1 configuration in ^{38}Ar is predominantly (93%) $\pi(d_{3/2})^2_{2^+}$ for which $g = +0.083$. This case demonstrates the extreme sensitivity of the magnetic moments to configuration mixing: the remaining 7% of the wave function raises the calculated moment to +0.308, in agreement with the experimental value [35]. It also shows the importance of off-diagonal terms (see Table VIII) as the diagonal contributions associated with the two main configurations account for only 60% of the total theoretical g factor.

Two neutrons have been added to the pf shell in the $N = 22$ isotones ^{38}S and ^{40}Ar. Because ^{36}S is almost doubly magic, the initial expectation might be that the first-excited state of ^{38}S would be dominated by the neutron $f_{7/2}$ configuration weakly coupled to the ^{36}S core, resulting in a g factor near −0.3. An example of this type of behavior is the $N = 52$ isotope $^{92}_{40}$Zr$_{52}$ [28,37]; the effect is also evident, but less pronounced, in $^{94}_{42}$Mo$_{52}$ [29]. In contrast with this weak-coupling scenario, the near-zero theoretical g factor and the small but positive experimental g factor of ^{38}S require additional proton excitations, which indicate strong

TABLE VI. Theoretical g factors compared with experiment.

Nuclide	Model	g^{th}_{proton}			$g^{th}_{neutron}$	g^{th}	g^{exp}
		Orbital	Spin	Total			
$^{36}_{16}$S$_{20}$	SDPF	0.967	0.187	+1.154	0	+1.154	
$^{38}_{16}$S$_{22}$	SDPF	0.225	0.073	+0.298	−0.301	−0.003	+0.13(5)[a]
	SDF	0.087	0.049	+0.136	−0.494	−0.358	
$^{40}_{16}$S$_{24}$	SDPF	0.225	0.051	+0.276	−0.241	+0.035	−0.01(6)[a]
	SDF	0.249	0.070	+0.318	−0.404	−0.085	
$^{38}_{18}$Ar$_{20}$	SDPF	1.151	−0.842	+0.308	0	+0.308	+0.24(12)[b]
$^{40}_{18}$Ar$_{22}$	SDPF	0.311	−0.147	+0.164	−0.364	−0.200	−0.02(4)[c]
	SDF	0.228	−0.092	+0.136	−0.431	−0.295	
$^{42}_{18}$Ar$_{24}$	SDPF	0.263	−0.043	+0.220	−0.280	−0.060	
	SDF	0.242	−0.025	+0.217	−0.417	−0.200	

[a]Present work.
[b]Reference [35].
[c]Reference [36].

TABLE VII. Partitions >5% contributing to the wave functions of the 2_1^+ states of ^{38}S and ^{40}S in the SDPF model.

Nuclide	Proton orbit			Neutron orbit				Occupation (%)
	$1d_{5/2}$	$1d_{3/2}$	$2s_{1/2}$	$1f_{7/2}$	$1f_{5/2}$	$2p_{3/2}$	$2p_{1/2}$	
^{38}S	6	0	2	2	0	0	0	26.89
	6	1	1	2	0	0	0	18.36
	6	2	0	2	0	0	0	12.10
	6	0	2	1	0	1	0	12.01
	6	1	1	1	0	1	0	6.36
^{40}S	6	2	0	4	0	0	0	17.26
	6	1	1	4	0	0	0	16.22
	6	0	2	4	0	0	0	9.30
	6	2	0	3	0	1	0	9.18
	6	1	1	3	0	1	0	8.37
	6	0	2	3	0	1	0	6.05

coupling between protons and neutrons. It is relevant to note that strong proton-neutron coupling is considered one of the prerequisites for the onset of deformation. The effect on the proton configuration due to coupling with neutrons in orbits above the $N = 28$ shell gap is discussed below.

For $N = 22, 24$ the shell model predicts a cancellation of the proton and neutron contributions to the moment. Under these conditions, the description of the g factors is satisfactory. The dependence of the $g(2^+)$ in ^{40}Ar on the basis space, the interaction, and the choice of effective nucleon g factors, has been investigated in Ref. [36]. To estimate the impact of the use of effective g factors, we recalculated the $g(2^+)$ values in Table VI adopting the effective g_l and g_s values employed by Stefanova *et al*. The effect was to make the 2^+-state g factors more positive, by ∼0.05 for the S isotopes and by ∼0.1 for the Ar isotopes; the discrepancy between theory and experiment for ^{38}S and ^{40}Ar is therefore reduced but not eliminated by the use of effective g factors.

A comparison may also be made between ^{38}S and ^{40}S, and their isotones ^{42}Ca and ^{44}Ca, where the experimental g factors, $g(2^+) = +0.04(6)$ and $g(2^+) = +0.16(3)$, are also far from that of the $\nu f_{7/2}^2$ configuration [38,39]. In both ^{42}Ca and ^{44}Ca there is evidently a significant collective component in the wave function that cannot readily be included in shell-model calculations [38,39]. Some remnant of this collective excitation may occur in ^{38}S and ^{40}S, although it is very much smaller than in the calcium isotopes.

TABLE VIII. Contributions to the g factors of the 2_1^+ states in ^{38}S, ^{40}S, ^{38}Ar, and ^{40}Ar for the SDPF model.

Orbits	^{38}S	^{40}S	^{38}Ar	^{40}Ar
$\pi 1d_{5/2}$–$1d_{5/2}$	0.046	0.067	0.044	0.033
$\pi 1d_{5/2}$–$1d_{3/2}$	−0.015	−0.003	0.124	0.003
$\pi 1d_{3/2}$–$1d_{3/2}$	0.014	0.014	0.080	0.021
$\pi 2s_{1/2}$–$2s_{1/2}$	0.254	0.199	0.061	0.107
$\nu 1f_{7/2}$–$1f_{7/2}$	−0.430	−0.447		−0.394
$\nu 1f_{7/2}$–$1f_{5/2}$	0.039	0.118		−0.002
$\nu 1f_{5/2}$–$1f_{5/2}$	0.009	0.011		0.005
$\nu 2p_{3/2}$–$2p_{3/2}$	0.054	0.092		0.018
$\nu 2p_{3/2}$–$2p_{1/2}$	0.026	−0.016		0.008
$\nu 2p_{1/2}$–$2p_{1/2}$	0.002	0.000		0.001

We conclude that the dominant components of the shell-model wave functions are correct and give a satisfactory description of the measured g factors. As such, the shell-model calculations provide a microscopic explanation of the development of quadrupole collectivity in these nuclei, which is now discussed in more detail.

The existence of deformation in nuclei has long been associated with strong interactions between a significant number of valence protons and neutrons, particularly in nuclei near the middle of a major shell. Without exception the deformed nuclei studied to date have g factors near the hydrodynamical limit, Z/A, reflecting the strong coupling between protons and neutrons, and a magnetic moment dominated by the orbital motion of the proton charge with small contributions from the intrinsic magnetic moments of either the protons or the neutrons. Examples include ^{24}Mg in the *sd* shell [40] and ^{50}Cr in the *pf* shell [41]. Robinson *et al*. [42] have recently used the shell model to examine the relation among the $B(E2)$ and $Q(2_1^+)$ and the orbital magnetic dipole strength (scissors mode) in these nuclei.

As noted above, Coulomb-excitation studies and the level scheme of ^{40}S suggest that it is deformed. Supporting this interpretation, the shell-model calculations (Table V) predict consistent intrinsic quadrupole moments when derived from either the $B(E2)$ or the quadrupole moment, $Q(2_1^+)$, implying a prolate deformation of $\beta \approx +0.3$, in agreement with the value deduced from the experimental $B(E2)$ [5]. The near-zero magnetic moment, however, does not conform to the usual collective model expectation of $g \sim Z/A$. Because the shell-model calculations reproduce both the electric and magnetic properties of the 2_1^+ state they give insight into the reasons for this unprecedented magnetic behavior in an apparently deformed nucleus.

The essential difference between the deformed neutron-rich sulfur isotopes and the deformed nuclei previously encountered (i.e., either light nuclei with $N = Z$ or heavier deformed

nuclei) is that the spin contributions to the magnetic moments are relatively more important, especially for the neutrons. It can be seen from Table VI that the proton contributions to the g factors are dominated by the orbital component, as is usually the case for deformed nuclei, but the substantial neutron contributions originate entirely with the intrinsic spin. The main partitions of the shell-model wave functions summarized in Table VII indicate that both ^{38}S and ^{40}S have a dominant occupation of the neutron $f_{7/2}$ orbit, for which $g = -0.547$ (unless coupled to spin zero). The net neutron contribution to the g factor in ^{38}S (^{40}S) is therefore $\sim$55%($\sim$44%) of that of a pure $f_{7/2}$ neutron configuration. Those configurations with neutron excitations into the $p_{3/2}f_{5/2}p_{1/2}$ shell mainly have a single occupation of the $p_{3/2}$ orbit. Although these excitations tend to reduce the magnetic moment of the neutrons from the value of the pure $f_{7/2}^n$ configuration, they do not cancel the neutron magnetic moment altogether because the g factor of the $\nu(f_{7/2} \otimes p_{3/2})_J$ configuration coupled to spin $J = 2$ is -0.183, and the value increases in magnitude for other possible values of J. The off-diagonal terms in the $M1$ operator also quench the $f_{7/2}$ neutron contribution to $g(2^+)$, as indicated in Table VIII.

The role of neutron excitations across the $N = 28$ shell gap can be examined further by comparing the calculations using the full SDPF model space with the truncated SDF calculations in which the neutrons were restricted to the $f_{7/2}$ shell. Looking first at the $E2$ properties presented in Table V, it is apparent from the $Q(2^+)$ values that excitations into the $p_{3/2}f_{5/2}p_{1/2}$ shell are needed to produce significant prolate deformations in ^{38}S and ^{40}S. Furthermore, in ^{40}S, the quadrupole moment and $B(E2)$ are not consistent with the same intrinsic quadrupole deformation unless the neutrons can occupy the $p_{3/2}f_{5/2}p_{1/2}$ shell. The wave functions in Table VII indicate that the development of quadrupole collectivity depends most sensitively on the occupation of the $\nu p_{3/2}$ orbit.

Turning to the g factors, it is apparent that two effects are important. First, in all cases the neutron contribution to $g(2^+)$ is quenched significantly when the $p_{3/2}f_{5/2}p_{1/2}$ orbits are occupied. Second, the case of ^{38}S shows a dramatic change in the g factor due to a relatively small neutron occupation of the $p_{3/2}$ orbit, highlighting that there is a strong coupling between the protons and neutrons. Specifically, a small occupation of the neutron $p_{3/2}$ orbit, moves the theoretical g factor from -0.358 to -0.003, falling short of the experimental value by a small margin compared with the distance traveled. Figure 15 shows how the proton partition of the wave function for ^{38}S changes significantly with the occupation of the $p_{3/2}f_{5/2}p_{1/2}$ shell; there is a significant increase in the contribution of the proton $s_{1/2}d_{3/2}$ configuration, which has a large g factor and which has been proposed to drive deformation. In contrast, Fig. 16 shows that for ^{40}S this proton configuration contributes strongly to the wave function whether or not excitations across the $N = 28$ gap are allowed. Apparently the effect of a single neutron occupying the $p_{3/2}$ orbit is diluted when three remain in the $f_{7/2}$ shell.

Because the hydrodynamical collective models fail to explain the g factor of ^{40}S, the observed quadrupole collectivity in this region is better interpreted in terms of the

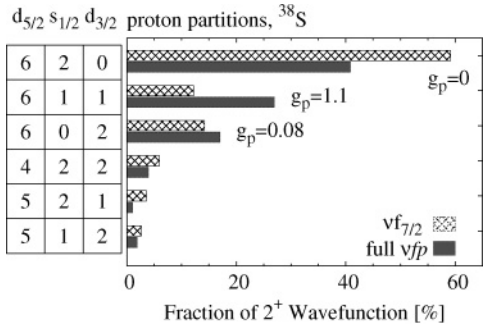

FIG. 15. Dominant proton partitions in ^{38}S comparing calculations in which neutrons occupy the full *pf* shell (SDPF) with calculations in which they are restricted to the $f_{7/2}$ shell (SDF). The g factors that represent the diagonal contributions of the most important configurations are indicated.

symmetries of the shell-model Hamiltonian. More specifically, the development of quadrupole collectivity can be linked to the quasi-SU(3) symmetry identified by Zuker *et al.* [43] and considered for the sulfur isotopes by Retamosa *et al.* [34]. In the neutron space the $\Delta j = 2$ orbits $f_{7/2}$-$p_{3/2}$ develop the quasi-SU(3) symmetry. As shown by the comparisons in Table V, occupation of the $p_{3/2}$ orbit is clearly essential if quadrupole collectivity is to emerge. Turning to the proton space, for the S isotopes of interest the proton $d_{5/2}$ orbit is essentially closed and only the $d_{3/2}$ and $s_{1/2}$ orbits are active (see Table VII). Although quasi-SU(3) cannot develop for these two orbits, an approximate pseudo-SU(3) geometry does develop. When neutrons begin to fill the *pf* shell, the effective energies of the two proton orbits become increasingly degenerate, as is manifested by the narrowing of the gap between the lowest $3/2^+$ and $1/2^+$ states in the odd-A isotopes of K, Cl, and P [10,44]. In the limit of degenerate $d_{3/2}$ and $s_{1/2}$ orbits the valence proton space has the geometry of pseudo-SU(3). Within this framework, quadrupole collectivity develops in the neutron-rich sulfur isotopes because the proton number is optimal for quadrupole coherence, despite the fact that the $d_{3/2}$-$s_{1/2}$ degeneracy is not reached [34].

The shift in the effective single-particle energies of the proton $d_{3/2}$ and $s_{1/2}$ orbits is strongly linked to the effect of the monopole component of the tensor term in the nucleon-nucleon interaction. Otsuka *et al.* [45] have shown that the effect of the monopole interaction between the proton $d_{3/2}$ and neutron $f_{7/2}$ orbits is attractive, which narrows the gap

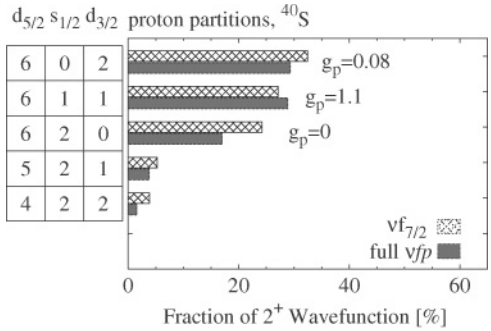

FIG. 16. As for Fig. 15, but for ^{40}S.

between the proton $d_{3/2}$ and $s_{1/2}$ states as more and more neutrons are added to the $f_{7/2}$ shell. This effect of the monopole interaction is therefore more pronounced in ^{40}S than in ^{38}S and may explain why the contribution of the proton partition $d^6_{5/2}s^1_{1/2}d^1_{3/2}$ is less sensitive to the neutron occupation of the $p_{3/2}$ orbit in ^{40}S than in ^{38}S.

V. SUMMARY AND CONCLUSION

In summary, we have developed a high-velocity transient-field technique to measure the g factors of excited states of neutron-rich nuclei produced as fast radioactive beams. The g factors of the first-excited states in the neutron-rich isotopes ^{38}S and ^{40}S have been measured with sufficient precision to test and challenge shell-model calculations.

Keys to the success of these measurements on low-intensity radioactive beams (10^4 to 10^5 pps) include (i) the use of intermediate energy Coulomb-excitation to align the nuclear spin and (ii) exploitation of the high velocities of the fragment beams to maximize the transient-field precession angle. In these measurements the precession angle per unit g factor is $\sim$10 times that in conventional measurements on neighboring nuclei [35,36,38,39].

The nature and origin of the quadrupole collectivity that develops between $N = 20$ and $N = 28$, including the role of excitations across the $N = 28$ shell gap, has been explored by comparing the measured g factors with shell-model calculations.

The case of ^{38}S highlights the role of strong proton-neutron interactions, showing that neutron excitations across the $N = 28$ shell gap cause a large change in the proton configuration. Taken together with the results for ^{40}S, it seems that excitations across the $N = 28$ shell gap *and* the reduction in the proton $s_{1/2}$-$d_{3/2}$ gap due to increasing neutron occupation of the $f_{7/2}$ orbit *both* contribute to the development of collectivity.

Because the hydrodynamical collective models fail to explain the g factor of ^{40}S, the observed quadrupole collectivity in this region should be interpreted in terms of the symmetries of the shell-model Hamiltonian. The unusual combination of magnetic and electric properties in ^{40}S apparently comes about because relatively few particles are involved in the collective motion. These features reemphasize the unique mesoscopic nature of the nucleus.

Looking to future applications of the high-velocity transient-field technique, it may be noted that the 2^+_1 state in the $N = 20$ nucleus $^{32}_{12}$Mg$_{20}$ has a similar excitation energy, lifetime and $B(E2)$ to ^{40}S. However the g factor in ^{32}Mg might be closer to that of a conventional collective nucleus because the $N = 20$ shell closure is known to vanish far from stability. Indeed a shell-model calculation using the interactions of Warburton, Becker, and Brown [46] gives $g = g_p + g_n = 0.52 - 0.11 = +0.41$, close to the collective value of $Z/A = 0.375$.

ACKNOWLEDGMENTS

We thank the NSCL operations staff for providing the primary and secondary beams for the experiment. We are grateful to Professor N. Benczer-Koller (Rutgers University) for performing the magnetometer measurement. This work was supported by NSF grants PHY-01-10253, PHY-99-83810, PHY-02-44453, and PHY-05-55366. A.E.S, A.N.W., and P.M.D. acknowledge travel support from the ANSTO AMRF scheme (Australia).

[1] A. D. Davies, A. E. Stuchbery, P. F. Mantica, P. M. Davidson, A. N. Wilson, A. Becerril, B. A. Brown, C. M. Campbell, J. M. Cook, D. C. Dinca *et al.*, Phys. Rev. Lett. **96**, 112503 (2006).
[2] A. E. Stuchbery, Phys. Rev. C **69**, 064311 (2004).
[3] A. D. Davies, A. E. Stuchbery, and P. F. Mantica (2006), to be published.
[4] S. Raman, C. W. Nestor, and P. Tikkanen, At. Data Nucl. Data Tables **78**, 1 (2001).
[5] H. Scheit, T. Glasmacher, B. A. Brown, J. A. Brown, P. D. Cottle, P. G. Hansen, R. Harkewicz, M. Hellström, R. W. Ibbotson, J. K. Jewell *et al.*, Phys. Rev. Lett. **77**, 3967 (1996).
[6] T. Glasmacher, B. A. Brown, M. J. Chromik, P. D. Cottle, M. Fauerbach, R. W. Ibbotson, K. W. Kemper, D. J. Morrissey, H. Scheit, D. W. Sklenicka *et al.*, Phys. Lett. **B395**, 163 (1997).
[7] J. A. Winger, P. F. Mantica, R. M. Ronningen, and M. A. Caprio, Phys. Rev. C **64**, 064318 (2001).
[8] D. Sohler, Z. Dombrádi, J. Timár, O. Sorlin, F. Azaiez, F. Amorini, M. Belleguic, C. Bourgeois, C. Donzaud, J. Duprat *et al.*, Phys. Rev. C **66**, 054302 (2002).
[9] T. R. Werner, J. A. Sheikh, W. Nazarewicz, M. R. Strayer, A. S. Umar, and M. Misu, Phys. Lett. **B335**, 259 (1994).
[10] P. D. Cottle and K. W. Kemper, Phys. Rev. C **58**, 3761 (1998).
[11] R. Rodríguez-Guzmán, J. L. Egido, and L. M. Robledo, Phys. Rev. C **65**, 024304 (2002).
[12] E. Caurier, F. Nowacki, and A. Poves, Nucl. Phys. **A742**, 14 (2004).
[13] T. Glasmacher, Annu. Rev. Nucl. Sci. **48**, 1 (1998).
[14] N. Benczer-Koller, M. Hass, and J. Sak, Annu. Rev. Nucl. Sci. **30**, 53 (1980).
[15] K.-H. Speidel, O. Kenn, and F. Nowacki, Prog. Part. Nucl. Phys. **49**, 91 (2002).
[16] D. J. Morrissey, B. M. Sherrill, M. Steiner, A. Stolz, and I. Wiedenhoever, Nucl. Instrum. Methods B **204**, 90 (2003).
[17] J. F. Ziegler, J. P. Biersack, and U. Littmark, *The Stopping and Range of Ions in Solids* (Permagon, New York, 1985).
[18] A. E. Stuchbery, A. D. Davies, and P. F. Mantica (2006), to be published.
[19] A. Piqué, J. M. Brennan, R. Darling, R. Tanczyn, D. Ballon, and N. Benczer-Koller, Nucl. Instrum. Methods A **279**, 579 (1989).
[20] W. F. Mueller, J. A. Church, T. Glasmacher, D. Gutknecht, G. Hackman, P. G. Hansen, Z. Hu, K. L. Miller, and P. Quirin, Nucl. Instrum. Methods A **466**, 492 (2001).
[21] K. L. Miller, T. Glasmacher, C. Campbell, L. Morris, W. F. Mueller, and E. Strahler, Nucl. Instrum. Methods A **490**, 140 (2002).
[22] C. A. Bertulani, A. E. Stuchbery, T. J. Mertzimekis, and A. D. Davies, Phys. Rev. C **68**, 044609 (2003).

[23] A. E. Stuchbery, P. M. Davidson, and A. N. Wilson, Nucl. Instrum. Methods B **243**, 265 (2006).
[24] G. Goldring, in *Heavy Ion Collisions*, edited by R. Bock (North-Holland, Amsterdam, 1982), Vol. 3, p. 484.
[25] A. E. Stuchbery, *Some notes on the program GKINT: Transient-field g-factor kinematics at intermediate energies*, Department of Nuclear Physics, The Australian National University, report no. ANU-P/1678 (2005); arXiv:nucl-ex/0609032 (2006).
[26] A. E. Stuchbery, Nucl. Phys. **A723**, 69 (2003).
[27] H. Olliver, T. Glasmacher, and A. E. Stuchbery, Phys. Rev. C **68**, 044312 (2003).
[28] G. Jakob, N. Benczer-Koller, J. Holden, G. Kumbartzki, T. J. Mertzimekis, K.-H. Speidel, C. W. Beausang, and R. Krücken, Phys. Lett. **B468**, 13 (1999).
[29] P. F. Mantica, A. E. Stuchbery, D. E. Groh, J. I. Prisciandaro, and M. P. Robinson, Phys. Rev. C **63**, 034312 (2001).
[30] A. E. Stuchbery, A. N. Wilson, P. M. Davidson, A. D. Davies, T. J. Mertzimekis, S. N. Liddick, B. E. Tomlin, and P. F. Mantica, Phys. Lett. **B611**, 81 (2005).
[31] B. A. Brown, A. Etchegoyen, N. S. Godwin, W. D. M. Rae, W. A. Richter, W. E. Ormand, E. K. Warburton, J. S. Winfield, L. Zhao, and C. H. Zimmerman, *Oxbash for Windows PC*, Michigan State University, report no. MSU-NSCL 1289 (2004).
[32] S. Nummela, P. Baumann, E. Caurier, P. Dessagne, A. Jokinen, A. Knipper, G. Le Scornet, C. Miehé, F. Nowacki, M. Oinonen *et al*., Phys. Rev. C **63**, 044316 (2001).
[33] E. Caurier, G. Martinez-Pinedo, F. Nowacki, A. Poves, and A. P. Zuker, Rev. Mod. Phys. **77**, 427 (2005).
[34] J. Retamosa, E. Caurier, F. Nowacki, and A. Poves, Phys. Rev. C **55**, 1266 (1997).
[35] K.-H. Speidel, S. Schielke, J. Leske, J. Gerber, P. Maier-Kormor, S. J. Q. Robinson, Y. Y. Sharon, and L. Zamick, Phys. Lett. **B632**, 207 (2006).
[36] E. A. Stefanova, N. Benczer-Koller, G. J. Kumbartzki, Y. Y. Sharon, L. Zamick, S. J. Q. Robinson, L. Bernstein, J. R. Cooper, D. Judson, M. J. Taylor *et al*., Phys. Rev. C **72**, 014309 (2005).
[37] A. E. Stuchbery, N. Benczer-Koller, G. Kumbartzki, and T. J. Mertzimekis, Phys. Rev. C **69**, 044302 (2004).
[38] S. Schielke, D. Hohn, K.-H. Speidel, O. Kenn, J. Leske, N. Gemein, M. Offer, J. Gerber, P. Maier-Komor, O. Zell *et al*., Phys. Lett. **B571**, 29 (2003).
[39] M. J. Taylor, N. Benczer-Koller, G. Kumbartzki, T. J. Mertzimekis, S. J. Q. Robinson, Y. Y. Sharon, L. Zamick, A. E. Stuchbery, C. Hutter, C. W. Beausang *et al*., Phys. Lett. **B559**, 187 (2003).
[40] B. A. Brown, J. Phys. G **8**, 679 (1982).
[41] R. Ernst, K.-H. Speidel, O. Kenn, A. Gohla, U. Nachum, J. Gerber, P. Maier-Komor, N. Benczer-Koller, G. Kumbartzki, G. Jakob *et al*., Phys. Rev. C **62**, 024305 (2000).
[42] S. J. Q. Robinson, A. Escuderos, L. Zamick, P. von Neumann-Cosel, A. Richter, and R. W. Fearick, Phys. Rev. C **73**, 037306 (2006).
[43] A. P. Zuker, J. Retamosa, A. Poves, and E. Caurier, Phys. Rev. C **52**, R1741 (1995).
[44] J. Fridmann, I. Wiedenhöver, A. Gade, L. T. Baby, B. D., B. A. Brown, C. M. Campbell, J. M. Cook, P. D. Cottle, E. Diffenderfer *et al*., Nature **435**, 922 (2005).
[45] T. Otsuka, T. Suzuki, R. Fujimoto, H. Grawe, and Y. Akaishi, Phys. Rev. Lett. **95**, 232502 (2005).
[46] E. K. Warburton, J. A. Becker, and B. A. Brown, Phys. Rev. C **41**, 1147 (1990).